SIAM J. Imaging Sciences
Vol. 18, No. 4, pp. 2159–2176

Iterative Filtering and Smoothing with Optical Flow Prediction Models*

Janne Hakkarainen[†], Zenith Purisha[‡], Neus Sabater[†], Monika Szeląg[†], Samuli Siltanen[§], and
Antti Solonen[¶]

Abstract. In this paper, we propose a new data assimilation approach based on iterative filtering and smoothing in the expectation-maximization fashion, incorporating optical flow prediction models for dynamic state estimation. The concept is suitable for applications where state estimation relies on two-dimensional images and where no natural physical prediction model is available. We apply the proposed approach to dynamic X-ray images and both real and synthetic satellite data, demonstrating that iterative filtering and smoothing with optical flow models yields improved results compared to using an identity model approach. The quality of the state estimates improves both visually and in terms of the root mean squared error, typically after a couple of iterations. However, in some cases, continued iterations may lead to deteriorating results. Therefore, monitoring the quality of both optical flow and state estimates is crucial in the iterative approach.

Key words. iterative filtering, Kalman filter, smoother, optical flow, data assimilation

MSC codes. 15A29, 65C60, 62M20, 60G35, 62F15

DOI. 10.1137/24M1689120

1. Introduction.

Kalman filtering, originally developed in the late 1950s and early 1960s, has gained popularity with a wide variety of applications from meteorology to engineering and beyond. One of its earliest applications was the trajectory estimation as part of the Apollo program's navigation computer [15]. Since the early days, several different variations and alternative formulations have been proposed [36]. Smoothers to postprocess the filtering results have also been proposed early on [34].

The central idea of filtering and smoothing is to recover a signal from noisy observations. They can also be used as a tool for parameter estimation. In some applications, filtering can be seen as a form of data assimilation and/or optimal interpolation between the model and the data. All in all, filtering and smoothing can be seen as a part of the Bayesian framework where the prior is updated to a state estimate using observations [36].

---

[*] Received by the editors August 29, 2024; accepted for publication (in revised form) June 16, 2025; published electronically October 8, 2025.

https://doi.org/10.1137/24M1689120

Funding: This work was funded by the Research Council of Finland (grants 353082, 359196, and 356937) and the Faculty of Mathematics and Natural Sciences, Universitas Gadjah Mada (grant 2469/UN1/FMIPA.1.3/KP/PT.01.03/2024).

[†] Finnish Meteorological Institute, Helsinki, FI-00101 Finland (janne.hakkarainen@fmi.fi, neus.sabater@fmi.fi, monika.szelag@fmi.fi).

[‡] Department of Mathematics, Universitas Gadjah Mada, Yogyakarta, 55281 Indonesia (zenith.purisha@ugm.ac.id).

[§] Department of Mathematics and Statistics, University of Helsinki, Helsinki, 00014 Finland (samuli.siltanen@helsinki.fi).

[¶] Department of Computational Science, LUT University, Lappeenranta, Finland and Danfoss Digital Services, Helsinki, 53850 Finland (antti.solonen@gmail.com).

In many physical applications, prediction is a central part of the filtering problem. This is particularly clear in numerical weather prediction (NWP), where the idea of data assimilation is to provide an initial state for predicting future weather. However, there are many data-driven applications where no (physical) prediction model is available. Filtering and smoothing can still be used for state and parameter estimation with empirical models. Notable applications are, for example, time series analysis with dynamic linear models [24], data fusion [17], and greenhouse gas flux estimation [32].

Optical flow is a standard technique to detect motion in machine vision [44] and the fundamental concepts were developed in the early 1980s [22, 25]. The basic approach is to calculate the motion field between consecutive images from a *reference* frame to a *target* frame [14]. In physical applications, optical flow algorithms are effective for short-term weather forecasting (nowcasting) as they are able to accurately track clouds across observed image series and predict forward trajectories and are generally applied to weather radar observations [38].

In this paper, we propose the idea of using optical flow prediction in iterative filtering and smoothing. The concept is motivated by using the expectation-maximization (EM) algorithm within the state estimation systems [11, 12, 10]. The proposed approach is aimed at applications with two-dimensional (2D) images (e.g., satellite, X-ray, and weather radar images) where no natural prediction model is available. Section 2 presents the methodology and section 3 applies it to practice. Finally, section 4 concludes this paper.

2. Methods.

2.1. Linear Gaussian filtering and smoothing.

Linear state-based model can be seen as the following pair:

$$\vec{x}_k = \mathbf{M}_k(\vec{x}_{k-1}) + \vec{\xi}_k, \tag{2.1}$$

$$\vec{y}_k = \mathbf{H}_k(\vec{x}_k) + \vec{\varepsilon}_k, \tag{2.2}$$

where $\mathbf{M}_k$ is the linear prediction model and $\mathbf{H}_k$ is the observation model that connects the state and the observations made at time step k. Model and measurement error terms $\vec{\xi}_k$ and $\vec{\varepsilon}_k$ are typically assumed to be zero-mean and Gaussian: $\vec{\xi}_k \sim N(\vec{0}, \mathbf{Q}_k)$ and $\vec{\varepsilon}_k \sim N(\vec{0}, \mathbf{R}_k)$. The model error covariance matrix $\mathbf{Q}_k$ is often static and simple (e.g., diagonal), and $\mathbf{R}_k$ is the observation error covariance matrix.

The state estimation problem is often solved with filtering by iterating the following two steps:

Prediction: The previous state estimate and its error covariance matrix are moved forward in time to become a priori estimate.

Update: Using observations, the prior is updated to become a state estimate.

The Kalman filter (KF) is a closed-form solution to the linear Gaussian filtering problem [36]. In the KF prediction step, we have

$$\vec{x}_k^{\mathrm{pr}} = \mathbf{M}_k \vec{x}_{k-1}^{\mathrm{est}}, \tag{2.3}$$

$$\mathbf{C}_k^{\mathrm{pr}} = \mathbf{M}_k \mathbf{C}_{k-1}^{\mathrm{est}} \mathbf{M}_k^{\mathrm{T}} + \mathbf{Q}_k. \tag{2.4}$$

The KF update step is most commonly written as

$$\vec{x}_k^{\text{est}} = \vec{x}_k^{\text{pr}} + \mathbf{K}_k(\vec{y}_k - \mathbf{H}_k\vec{x}_k^{pr}), \tag{2.5}$$

$$\mathbf{C}_k^{\text{est}} = (\mathbf{I} - \mathbf{K}_k\mathbf{H}_k)\mathbf{C}_k^{pr}, \tag{2.6}$$

$$\mathbf{K}_k = \mathbf{C}_k^{pr}\mathbf{H}_k^{\mathrm{T}}(\mathbf{H}_k\mathbf{C}_k^{pr}\mathbf{H}_k^{\mathrm{T}} + \mathbf{R}_k)^{-1}, \tag{2.7}$$

where $\mathbf{K}_k$ is the Kalman gain matrix at time step k. However, alternative formulations exist. In the case of the nonlinear models $\mathcal{M}_k$ and $\mathcal{H}_k$, a nonlinear version of the KF, such as the extended Kalman filter (EKF), can be used [36].

The Rauch–Tung–Striebel smoother (RTSS) is the corresponding closed-form smoother for linear Gaussian state space models [36]. One starts from the final KF state estimate and operates recursively:

$$\vec{x}_{k-1}^{\text{smooth}} = \vec{x}_{k-1}^{\text{est}} + \mathbf{C}_{k-1}^{\text{est}}\mathbf{M}_k^{\mathrm{T}}(\mathbf{C}_k^{\text{pr}})^{-1}(\vec{x}_k^{\text{smooth}} - \vec{x}_k^{\text{pr}}). \tag{2.8}$$

Also, the error covariance matrix $\mathbf{C}_{k-1}^{\text{smooth}}$ can be obtained recursively:

$$\begin{aligned}\mathbf{C}_{k-1}^{\text{smooth}} = \mathbf{C}_{k-1}^{\text{est}} + \mathbf{C}_{k-1}^{\text{est}}\mathbf{M}_k^{\mathrm{T}}(\mathbf{C}_k^{pr})^{-1}(\mathbf{C}_k^{\text{smooth}}\\ - \mathbf{C}_k^{\text{pr}})(\mathbf{C}_k^{pr})^{-1}\mathbf{M}_k\mathbf{C}_{k-1}^{\text{est}},\end{aligned} \tag{2.9}$$

although, this error covariance matrix is not needed for calculating the state estimate.

In this paper, we apply the KF and RTS smoother to a series of two-dimensional (2D) images $\vec{x}_k$. If the dimensions of the images are even moderately high—for example, $N \times N$—handling or even storing the covariance matrices, which are of size $N^2 \times N^2$, becomes challenging in practice. Therefore, in practical calculations, we apply the dimension reduction approach described in Appendix A.

2.2. Optical flow.

One of the most widely used approaches for estimating motion between consecutive images is optical flow [44]. The foundational principle for optical flow estimation is the brightness constancy assumption, which posits that the intensity of a point in an image remains constant over a short time interval despite its motion. Mathematically, for an image intensity function $I(x, y, t)$, this is expressed as

$$I(x, y, t) = I(x + u, y + v, t + 1). \tag{2.10}$$

For small displacements, applying a first-order Taylor expansion to the right-hand side and neglecting higher-order terms yields the optical flow constraint equation:

$$\frac{\partial I}{\partial x}u + \frac{\partial I}{\partial y}v + \frac{\partial I}{\partial t} = 0, \tag{2.11}$$

where $\partial I/\partial x$ and $\partial I/\partial x$ are the spatial gradients of the image intensity, and $\partial I/\partial t$ is the temporal gradient. This equation, often written as $I_x u + I_y v + I_t = 0$, forms the basis of classical optical flow methods. However, it is underconstrained, providing one equation for two unknowns (u and v), a problem known as the aperture problem. To resolve this, additional assumptions are introduced, such as spatial smoothness, as in the Horn–Schunck method [22], which minimizes an energy functional:

$$E = \iint \left((I_x u + I_y v + I_t)^2 + \alpha(|\nabla u|^2 + |\nabla v|^2)\right) dx\, dy, \tag{2.12}$$

where α is a regularization parameter balancing data fidelity and smoothness, and ∇u and ∇v are the gradients of the flow components. Alternatively, the Lucas–Kanade method [25] assumes local constancy of flow within a small neighborhood, solving a system of equations derived from multiple pixels.

In this paper, the optical flow calculations are performed using the large displacement optical flow based on [4, 5]. We use an external MATLAB toolbox (https://www.cs.cmu.edu/∼katef/LDOF.html) with an off-the-shelf setup. The toolbox employs a coarse-to-fine variational approach for optical flow estimation between image frames, integrating descriptor matches alongside traditional brightness and gradient constancy constraints to effectively handle significant displacements of both small and large structures.

2.3. Iterative filtering and smoothing with optical flow prediction. To utilize Kalman filtering (or smoothing) for parameter estimation, one approach involves forming a "filter likelihood" [20, 40]. Another option is to apply the Expectation-maximization (EM) approach within the filtering process [27] as demonstrated in prior studies [12, 10]. The EM approach is based on two steps:

Expectation-step: Operate the KF (and/or smoother) with current parameters to calculate the state estimates $\vec{x}_k$.

Maximization-step: Using the updated state estimates, calculate new parameter estimates.

In this paper, we work in the context where we do not have the prediction model $\mathcal{M}_k$ available, which is quite a typical starting point for data-driven applications. Here, we use the EM approach in the context of optical flow and 2D images. Previously, the EM approach has been used to estimate a static linear prediction model $\mathbf{M}_k = \mathbf{M}$ [11].

In the optical flow method, the displacement field is calculated between two discrete images $\vec{x}_{k-1}$ and $\vec{x}_k$. This displacement field offers a linear model $\mathbf{M}_k^{\text{flow}}$ that can be used to warp between images, which is essentially what is needed for linear Kalman filtering (when the actual model is not known). The image $\vec{x}_k$ is not typically available before the KF prediction (and update) are performed. This motivates us to propose the following iterative approach:

Expectation-step: Operate the KF (or smoother) with current models $\mathbf{M}_k$ to calculate the state estimates $\vec{x}_k$.

Maximization-step: Using optical flow with updated state estimates $\vec{x}_k$, define models $\mathbf{M}_k = \mathbf{M}_k^{\text{flow}}$.

Figure 1 illustrates how the iterative filtering and smoothing approach works. A practical choice for the iteration 0 is to use $\mathbf{M}_k = \mathbf{I}$.

We note that standard optical flow methods typically operate between two consecutive images. However, there is no fundamental reason why this should be the case here, as all images are available after state estimation. In fact, recent work [37] describes multiframe optical flow estimation. Similar ideas, where motion fields are estimated from an image sequence, have been discussed in the context of dynamic X-ray tomography [7].

In principle, the approach is expected to have the *virtuous circle*: better state estimates create better models, and better models create better state estimates, and so on. On the other hand, also the *vicious circle* is possible: if the state estimates become worse at some iteration, then the models become worse, which creates worse state estimates, etc. In practical terms, the quality of the optical flow and the state estimates has to be closely monitored.

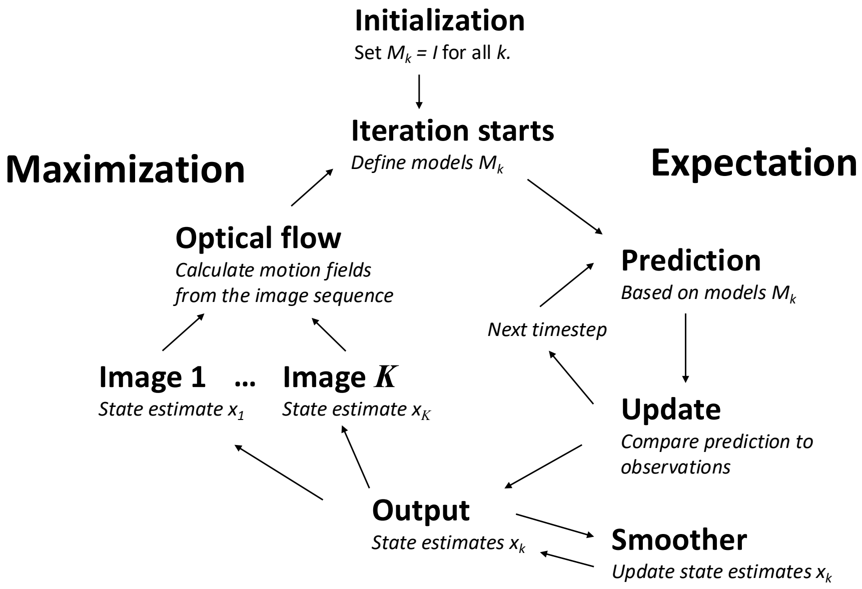

Figure 1. *Illustration of iterative filtering and smoothing with optical flow techniques.*

We note that the regularization offered by the optical flow method is critical for the approach to work in practice. In an extreme case where no regularization is applied to the models $\mathbf{M}_k$, the EM approach could simply predict the current observations $\vec{y}_k$ from the previous observations $\vec{y}_{k-1}$ and converge to $\vec{x}_k = \vec{y}_k$, assuming identity observation operators $\mathbf{H}_k = \mathbf{I}$.

Remarks:

- The proposed approach is aimed at quite specific applications. The state estimation is done between 2D images where no dynamical model is available. In some applications, optical flow can be applied for layers of "three-dimensional (3D) images," although 3D scene flow exists too [47].
- Optical flow might be unstable in the initial stages of filtering if the quality of the state estimates is poor. In such cases, it might be advantageous to initiate the optical flow only after the filter has converged and use, for example, $\mathbf{M}_k = \mathbf{I}$ before that.
- Optical flow works with the assumption of brightness constancy (no sources or sinks) and that the movement is small. Even if the state estimates $\vec{x}_k$ are known perfectly, the models $\mathbf{M}_k^{\text{flow}}$ are hardly perfect.
- For the sake of readability, we presented the theory in a very general framework. One could try and implement these ideas with their favorite filtering and optical flow algorithms.

3. Results.

3.1. Case study 1: Dynamic X-ray tomography. Computed tomography (CT) is a noninvasive imaging technique widely used across various fields to visualize the internal structure of an object by passing X-rays through it from multiple angles or projections. Dynamic CT imaging, on the other hand, involves reconstructing image sequences with a focus on capturing the temporal changes of the target [3]. This approach aligns with state estimation, where 2D images are used without the availability of a dynamical model [7].

Here, we reanalyze the emoji case study from [21] with dimension reduction KF and RTS smoother. The dataset was measured at the University of Helsinki and publicly available online; see [26] for details. The stop-motion emoji dataset consists of 33 time steps with 60 angular directions out of 360°. We use a target image size of 128×128 with 2,704 basis vectors.

The first column of Figure 2 shows the Tikhonov regularization "target images" with 60 angular directions. For the dynamic state estimation, we use 10 angular directions. In this paper, the mathematical model of the dynamic X-ray tomography can be seen in [21].

First, we select identity forward models $\mathbf{M}_k = \mathbf{I}$. This iteration 0 is shown in the second column of Figure 2. Altogether, we perform 20 iterations. After each iteration, for $k = 5,\dots,33$, we define new models $\mathbf{M}_k^{\text{flow}}$, calculated between the images $\vec{x}_{k-1}$ and $\vec{x}_k$. For time steps 2–4, we use the identity forward models. Kalman filtering results with the optical flow models calculated from the 60-angle Tikhonov regularization images are shown in the rightmost column of Figure 2. The supplementary material (M168912_01.pptx [local/web 119MB]) includes a full animation for iterations 4 and 20.

Figure 3 presents the corresponding flow fields, which represent velocity distributions over space. The rightmost column displays the one derived from the 60-angle Tikhonov regularization images. Among the iterations, the result at iteration 4 exhibits the closest resemblance to this reference. The movement of the emoji face's eyes and mouth is clearly visible. Additionally, the intensity increases notably at iterations 10 and 20, which is already evident in the iteration 20 reconstructions in Figure 2.

Figure 4a shows the RMSE as a function of time steps. The RMSE is calculated against the full Tikhonov regularization images. Figure 4b shows the mean RMSEs calculated between steps 10–33. Vertical lines indicate results calculated with "Tikhonov regularization models." For both filtering and smoothing, the optimum is found at around iteration 4 or 5, but the results deteriorate afterward. This can be visually seen also from the X-ray images presented in Figure 2. The visual effects at iteration 4 have improved compared to iteration 0 (e.g., the left eye of the emoji face), but at iteration 20, we see clear artifacts caused by the optical flow models. The smoothing results are quite similar to the filtering results, although the mean RMSE is slightly higher. However, the smoothing drastically improves the results at iteration 0 at the beginning of the state estimation process. Here, we calculated the optical flow from the Kalman filtering state estimates. Calculating the optical flow from the RTS smoothing estimates produces slightly higher RMSEs but significantly slower convergence. The optimum is reached only after about 100 iterations (not shown in figures).

Based on visual inspection, the results calculated with "Tikhonov regularization models" likely show the sharpest and closest resemblance to the full Tikhonov regularization reconstructions, as expected. Interestingly, this setup does not yield the overall lowest RMSE. In fact, Figure 4a shows that it provides the lowest RMSE around iteration 10, but the RMSE starts increasing afterward. The reason is that, despite visual agreement, the absolute difference between the two reconstructions above the emoji face is larger here than with the optimal setup. One reason for this is that the chosen KF parameters, such as the static model

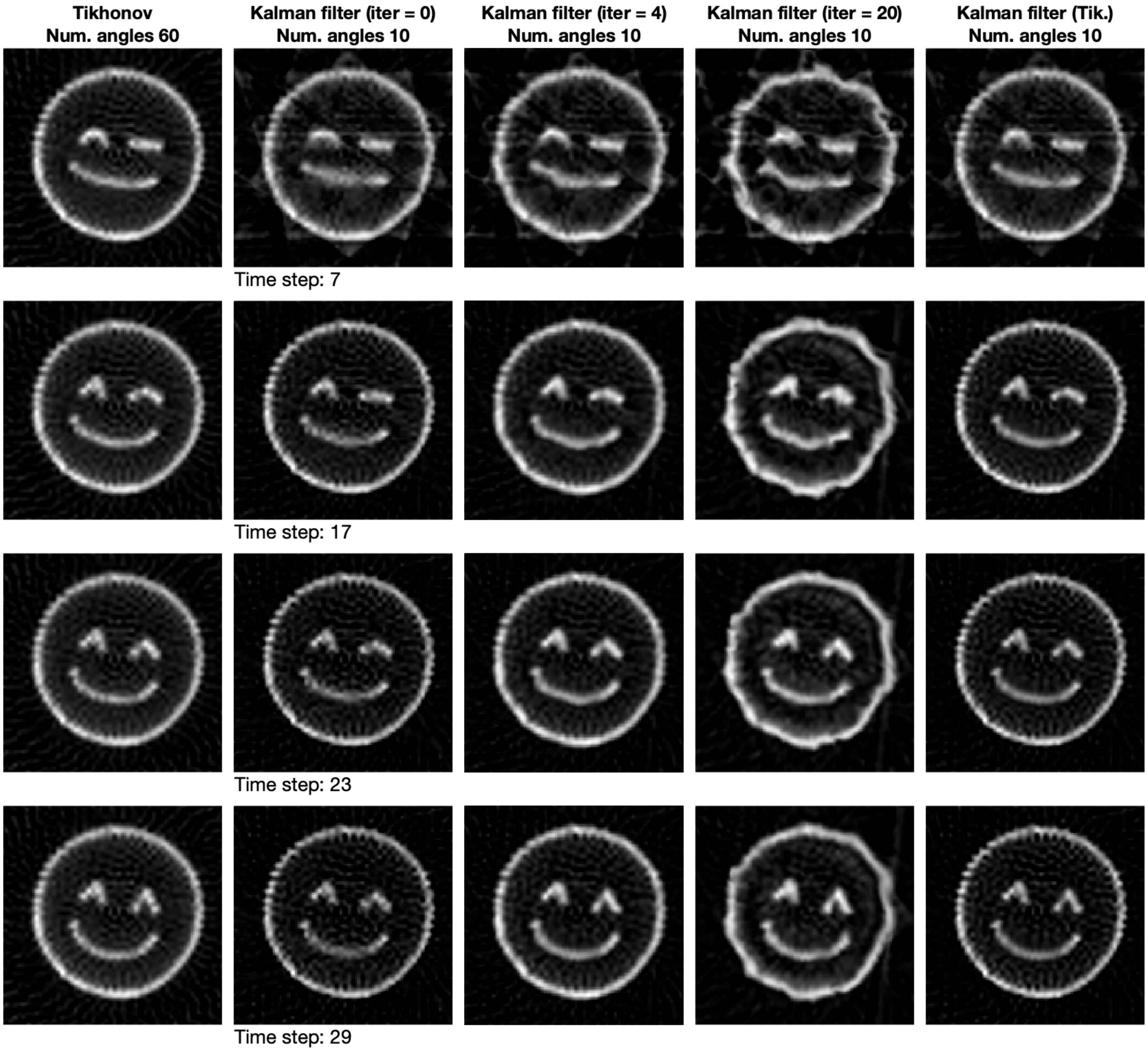

Figure 2. *The first column displays* 60*-angle Tikhonov regularization reconstructions of the emoji face at different time steps* (7, 17, 23, 29)*. The remaining columns show filtering results with various setups, each setup indicated in the title.*

error covariance matrix $\mathbf{Q} = 0.1^2 I$, are more optimal for other models. If this parameter is decreased, the overall RMSE decreases for all models but generally produces inferior results at the beginning of the simulation (not shown in figures). In real-life applications, a potential way to tune $\mathbf{Q}$ is to analyze the prediction residuals $r_k = \vec{y}_k - \mathbf{H}_k \vec{x}_k^{\text{pr}}$. Moreover, in these types of applications, having two sets of model error covariance matrices—one used before convergence and the other used after—might be beneficial.

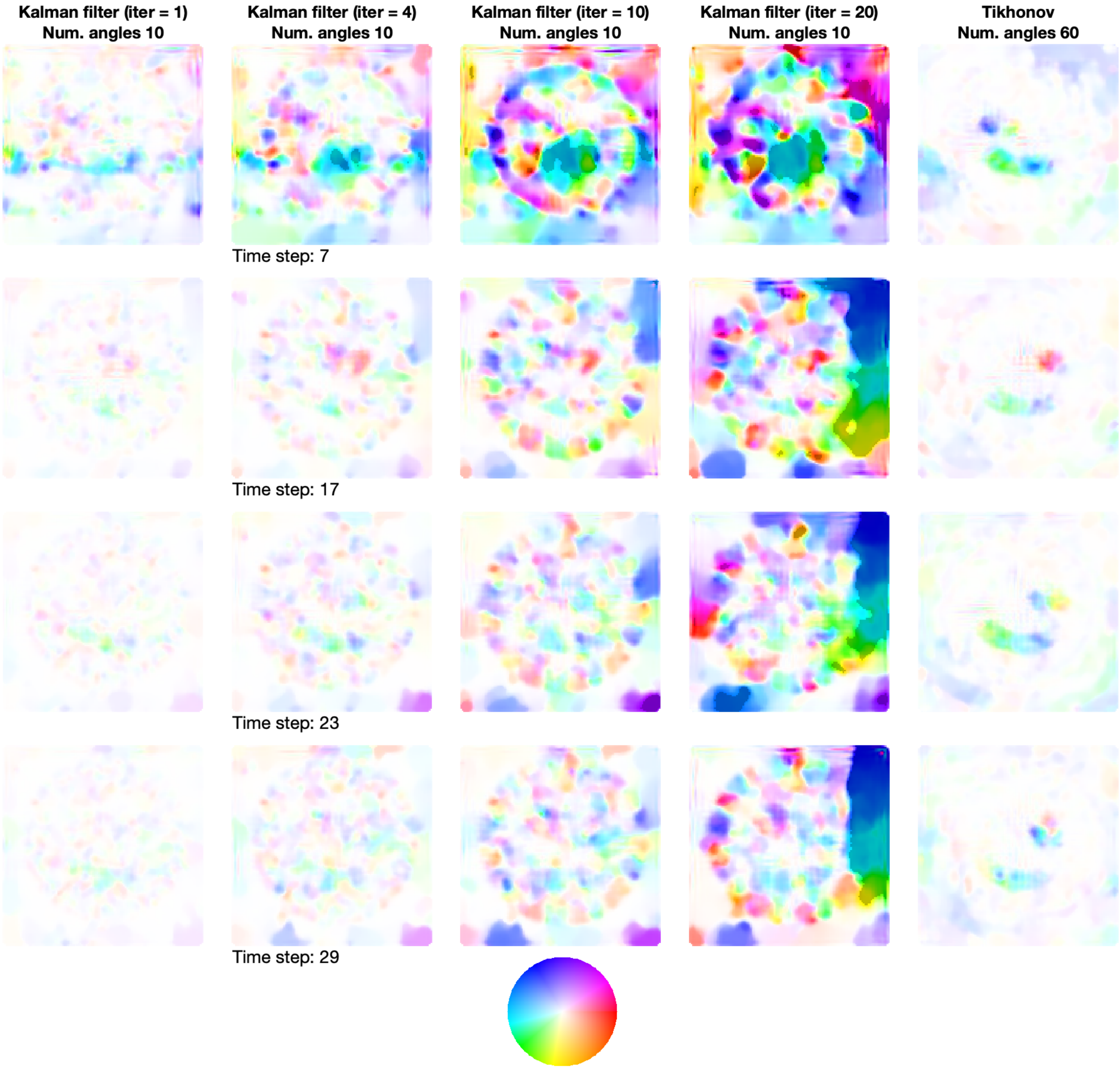

Figure 3. *The emoji face flow fields for different KF iterations at time steps* 7*,* 17*,* 23*, and* 29*. The rightmost column shows the flow fields calculated from the* 60*-angle Tikhonov regularization reconstructions. Colors indicate flow direction, while color intensity represents flow magnitude (see color wheel for reference).*

3.2. Case study 2: CO_2 state estimation. In climate science, space-based carbon dioxide (CO_2) observations are typically assimilated using an *inverse modeling* approach [32], where the CO_2 fluxes (sources and sinks) are updated based on the atmospheric data. State estimation has been proved useful when analyzing year-to-year differences [48].

To create synthetic experiments, we utilize the global chemical transport model GEOS-Chem version 12.9.1 (www.geos-chem.org). Further details are provided in Appendix B. The assimilation study is conducted on a daily basis at 12 UTC for one year, covering the area

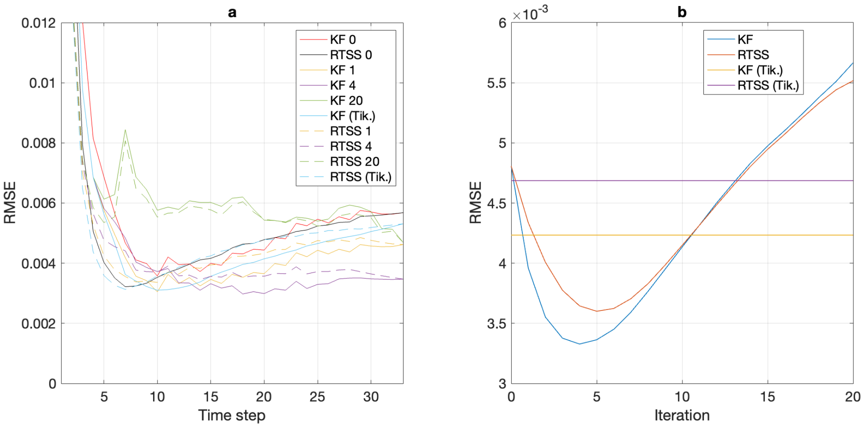

Figure 4. *Panel* a *displays the root mean squared error (RMSE) of the emoji case as a function of time steps for various setups. Panel* b *shows the mean RMSE from time steps* 10–33*. Vertical lines indicate the results obtained with Tikhonov regularization models.*

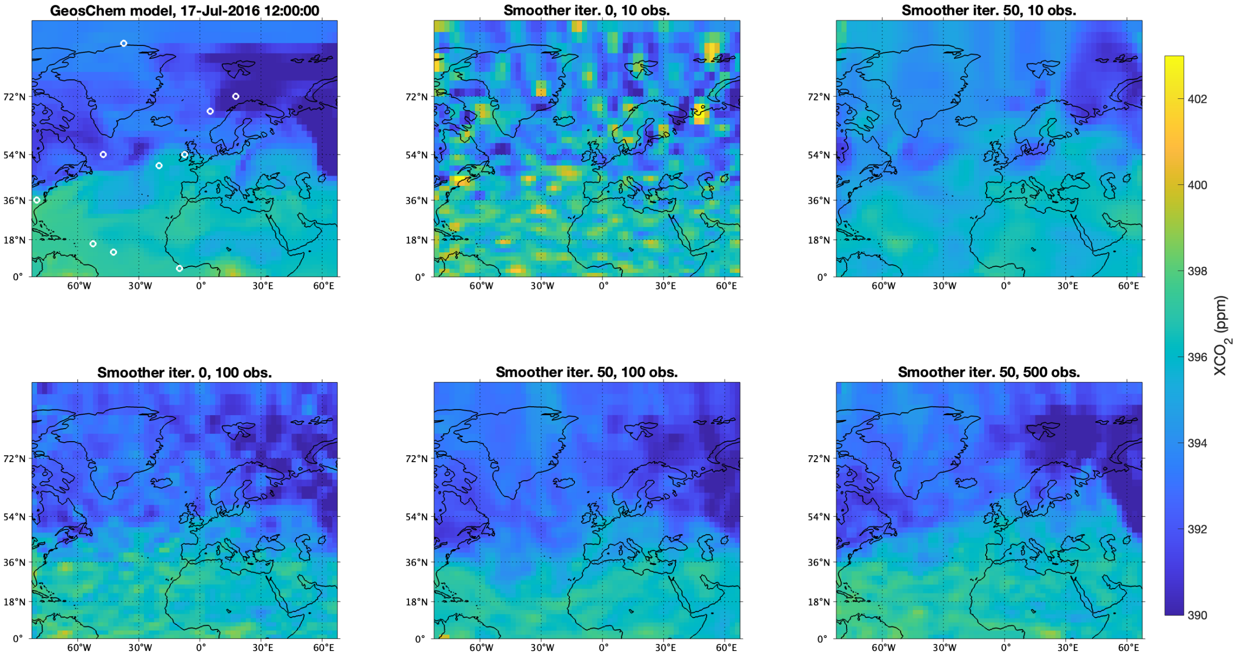
GeosChem model, 17-Jul-2016 12:00:00

Smoother iter. 0, 10 obs.

Smoother iter. 50, 10 obs.

Smoother iter. 0, 100 obs.

Smoother iter. 50, 100 obs.

Smoother iter. 50, 500 obs.

Figure 5. *The first panel displays the GEOS-Chem model simulations on July* 17*,* 2016*. White circles indicate* 10 *observations. The remaining panels show smoothing results with different numbers of iterations (*0 *and* 50*) and observations (*10*,* 100*, and* 500*). Each setup is indicated in the title.*

illustrated in Figure 5. We generate synthetic data by sampling different numbers of observations (10, 100, and 500) at random simulation locations (which vary from time point to time point) and add random noise of 1 ppm. The observational quantity is the column-averaged CO_2 dry air mole fraction, XCO_2 (as would observed by a satellite). These types of observation are produced by the GOSAT satellite [51].

We start the iterations with identity models (iteration 0) and perform a total of 50 iterations with different setups. Figure 7 shows the mean RMSEs calculated against the GEOS-Chem simulations. Vertical lines indicate the mean RMSEs using the optical flow models calculated from the GEOS-Chem simulations. The overall level of RMSEs depends on the number of observations. With just ten observations, the optimum is reached after about 30 iterations. With 100 and 500 observations, the optimum is reached only after a couple of iterations. With 500 observations, the RTS smoothing using identity models performs the best.

Figure 5 shows a snapshot of different smoothing state estimates on July 17, 2016. Using the identity models with 10 observations (top row, middle panel) reveals large deviations from the GEOS-Chem simulations (top row, left panel). Additionally, the locations of the assimilated observations can be visually detected. In this case, the iterative approach with optical flow models significantly improves the quality (top row, right panel). With 100 observations, the improvement is still visible but less drastic (bottom row, left, and middle panels). With 500 observations (bottom row, right panel), the details are further improved compared to the simulations. The supplementary material (M168912_01.pptx [local/web 119MB]) includes an animation for iterations 1 and 25, each with 100 observations.

Figure 6 shows the optical flow fields on July 17, 2016. The first panel presents the optical flow calculated from the true GEOS-Chem fields, while the others show results using 10, 100, and 500 observations at iterations 25 and 50. At first glance, the flow fields appear very different from one another. The closest resemblance to the GEOS-Chem flow field is

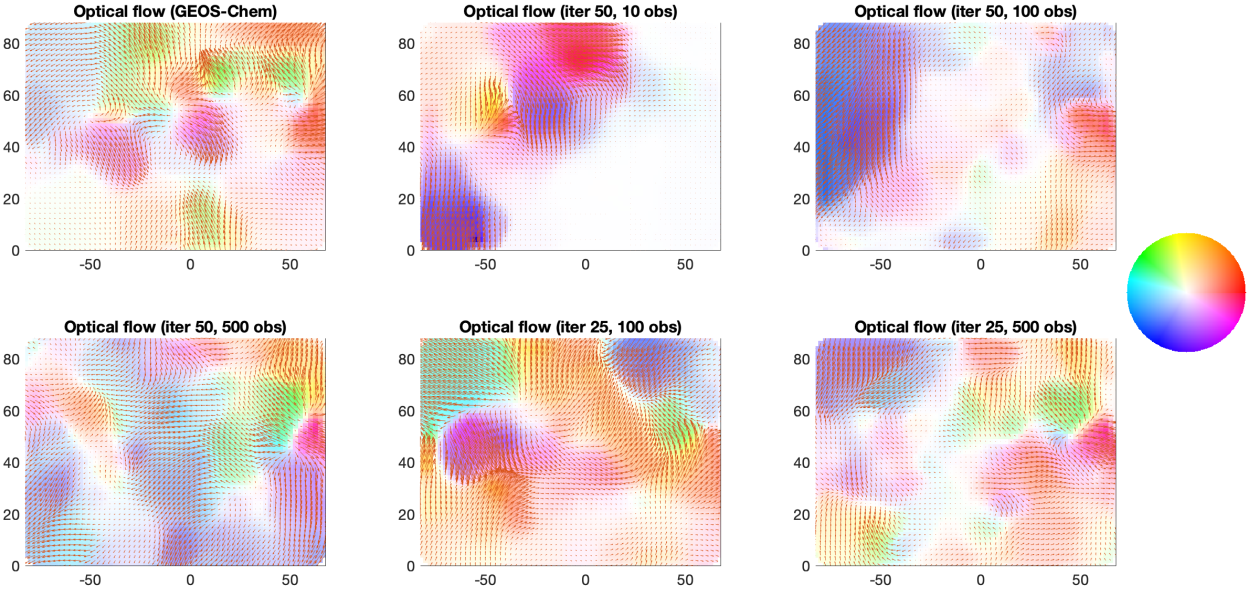

Figure 6. *Optical flow fields on July 17, 2016. The first panel presents the optical flow calculated from the true GEOS-Chem fields, while the others show results using 10, 100, and 500 observations at iterations 25 and 50. Colors indicate flow direction, while color intensity represents flow magnitude (see color wheel for reference).*

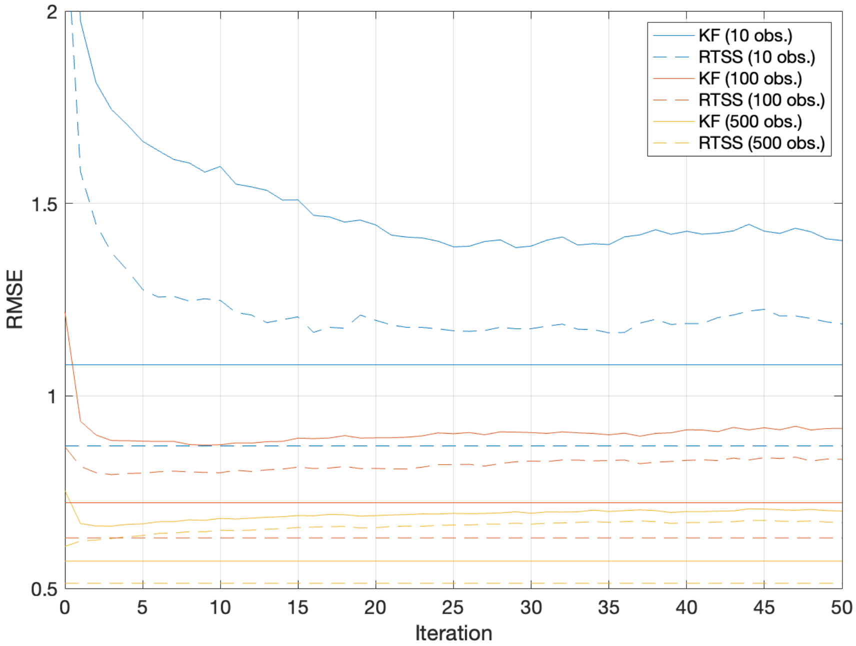

Figure 7. *The RMSE as a function of iteration in the iterative KF with different numbers of observations (*10, 100, *and* 500*) used. Vertical lines indicate the RMSE using flow models calculated from the GEOS-Chem simulations.*

likely obtained with 500 observations at iteration 25. With 10 observations, the area where observations are available is clearly highlighted, whereas the region without any observations shows virtually no flow. Overall, the results highlight the difficulty of obtaining a realistic flow field. We note that the flow itself also varies significantly between iterations 25 and 50, even when the change in RMS errors is less drastic.

Here again, we calculated the optical flow from the Kalman filtering state estimates. Calculating the optical flow from the RTS smoothing estimates yields similar results, albeit with slightly worse RMSEs. This effect is most pronounced with just 10 observations, as expected (not shown in the figures).

3.3. Case study 3: Filling gaps of space-based SIF data. Solar-induced chlorophyll fluorescence (SIF) is the radiance signal emitted by chlorophyll molecules in plants as a dissipation mechanism after they absorb sunlight. Given its dependency on the absorbed sunlight, it has been exploited as a proxy for vegetation gross primary production, GPP [43], which is defined as the synthesis of organic compounds from atmospheric CO_2, primarily occurring through the process of photosynthesis.

We utilize the TROPOSIF global sun-induced fluorescence dataset from the Sentinel 5 Precursor TROPOMI mission (https://s5p-troposif.noveltis.fr/ [16, 29]) at 743 nm. Using the KF, the goal is to create a continuous dataset and fill in the gaps due to clouds and other artifacts. While there are models to predict the emitted SIF signal given a set of parameters definitions [49, 13], to the best of the authors' knowledge, there is no dynamical model that would predict the current state $\vec{x}_k$ from the previous state $\vec{x}_{k-1}$. Unlike atmospheric

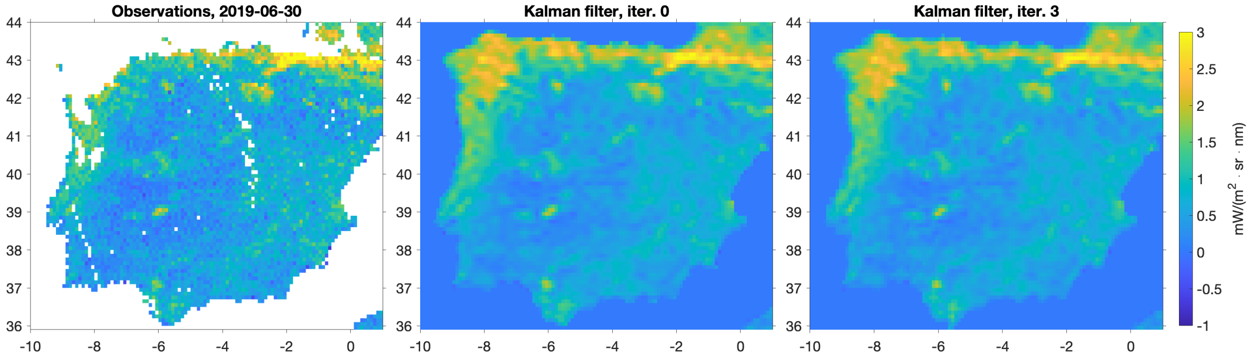

Figure 8. *The left panel displays the TROPOSIF observations over the Iberian Peninsula on June* 30*,* 2019*. The middle panel shows filtering results with identity models (iteration* 0*), and the right panel with optical flow models (iteration* 3*).*

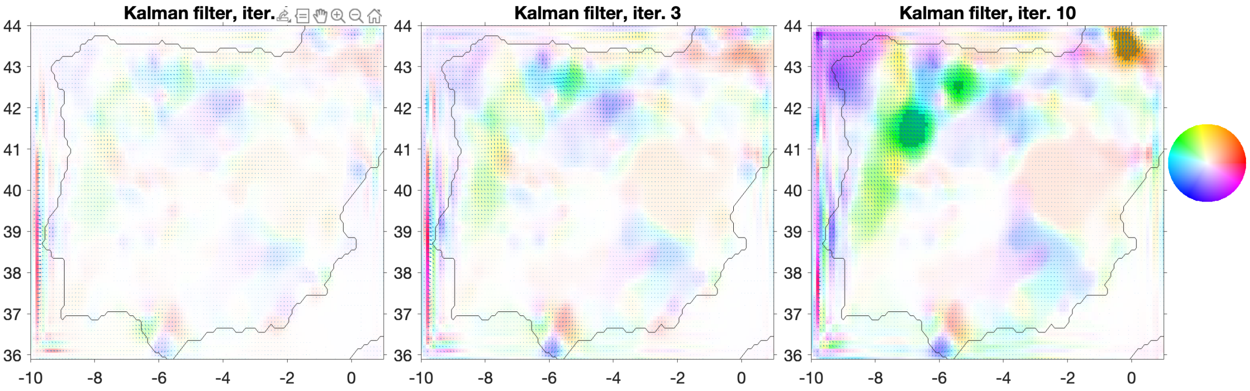

Figure 9. *Flow fields for different KF iterations over the Iberian Peninsula on June* 30*,* 2019*. Colors indicate flow direction, while color intensity represents flow magnitude (see color wheel for reference).*

components such as CO_2 concentration, whose dynamics can be evidently modeled using transport models, the role of transport models in SIF is less immediately apparent. Although plants' locations are static, SIF emission is influenced by atmospheric fields, primarily solar radiation, temperature, and water vapor availability [9, 8]. Consequently, while transport modeling may seem less intuitive for SIF, it can be understood due to the indirect dependency on these atmosphere-related fields.

Here, we assimilate the TROPOSIF data over the Iberian Peninsula for the year 2019. We start the assimilation process with an identity model using observation and model errors of 1 mW/(m^2·sr·nm). Figure 8 shows a snapshot of the observations and the assimilation results on June 30, 2019. Figure 9 presents the corresponding flow fields.

In this example, we do not have any verification data available. Instead, we monitor the prediction residuals $r_k = \vec{y}_k - \mathbf{H}_k \vec{x}_k^{\text{pr}}$ and their sum of square. Figure 10a shows the sum of squares as a function of the day of the year. We note that even though the sum of squares is highest during the summer months, the relative prediction residuals are lower because photosynthesis is most active. Overall, the optical flow KF has improved the prediction

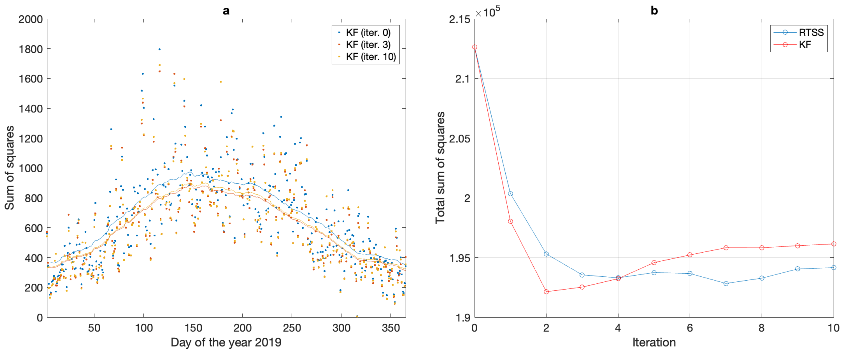

Figure 10. *Panel* a *displays the sum of squares of the prediction residual as a function of time. Solid lines indicate* ±*50-day moving average. Panel* b *displays the total sum of squares of the prediction residuals as a function of iteration using the KF and RTS smoother optical flow models.*

residuals with respect to the identity model filter. Figure 10b shows the total sum-of-squares as a function of iteration using both KF and RTS smoother optical flow models. It is worth noting that, in absolute terms, the differences are not very high between both options. With the KF optical flow models, the optimum is reached after two or three iterations, and the total sum of squares slightly increases thereafter. In contrast, with RTS smoother optical flow models, no clear optimum is found; however, after iteration 4, the total sum of squares is smaller than that obtained with KF optical flow models.

Visually, we observe only minor differences between iterations 0 and 3 (Figure 8), and in both cases, we can create a full image even in regions where there is no data available. However, it is important to note that filled data may not be representative of the true SIF under cloudy conditions. Plants' emission of SIF under sunlit and shade conditions differ [52], and with a data assimilation scheme, predictions are made by taking a previous step where there was artifact- and cloud-free data. Thus, the proposed approach used here is only able to fill in small data gaps in the temporal and spatial domain. For example, the large data gaps occurring during the polar night cannot be filled. The supplementary material (M168912_01.pptx [local/web 119MB]) includes an animation for iterations 0 and 3. From the flow field (Figure 9), we observe the apparent "motion" of SIF, which may result from a combination of atmospheric factors—such as solar radiation, temperature, vapor pressure deficit, and latent and sensible heat—as well as intrinsic variations in the SIF emission signal. On this day, clear artifacts are also visible near the edges of the image. Additionally, we note that the intensity of the flow increases at iteration 10; however, in general, the patterns in the flow fields remain similar across iterations.

4. Concluding remarks.

In this paper, we proposed iterative filtering and smoothing algorithms with optical flow prediction models. The iterations are motivated by the EM approach. In most cases, we observe improvements compared to the identity models only after a couple of iterations. However, these improvements do not necessarily persist indefinitely; in some cases, optical flow can produce clear artifacts and deteriorate image quality. We emphasize the need for quality control of state and optical flow estimation in all applications.

In the first two case studies, we found the best results in terms of RMSE using optical flow between filtering rather than smoothing-based state estimates. This result may be expected, as filtering generally exhibits more "dynamic" behavior compared to smoothing, although there may be applications where it is preferable to use smoothing-based state estimates.

The first case study in this paper was based on measured X-ray images of an emoji. Similar real-world applications are available in dynamic medical imaging [31], wood log tomography [42], and plant studies [6].

The second case study was based on synthetic satellite CO_2 observations. While this example is somewhat artificial due to the availability of dynamical atmospheric models, data-driven CO_2 applications exist as well [19, 18], and most satellite image applications lack natural dynamic models. Space-based CO_2 observations are commonly used in inverse modeling. In our case study, we used point-like observations similar to those observed by, for example, the GOSAT satellite. In the future, new satellite observations with improved mapping capabilities will become available [23]. The third case study involves filling gaps in space-based SIF data where no underlying model is available. Besides gap-filling, the proposed technique could enable more continuous monitoring of plants' status by detecting subtle deviations in SIF that may indicate early stress conditions, such as water limitations or heat stress, before they manifest in traditional optical remote sensing vegetation indices. Similar applications have been considered, for example, in water quality monitoring [17]. For global applications, it is not immediately clear how to apply optical methods on a sphere or with images with symmetric boundaries. Finally, we note that both the CO_2 and SIF case studies clearly violate the optical flow assumption of brightness constancy (i.e., no sources or sinks) in long-term analyses. Nevertheless, in day-to-day analyses, this violation is less pronounced.

In all case studies, the quality of the state estimates improves both visually and in terms of RMSE. The situation is less clear for the flow fields, except perhaps for the emoji example. Estimating realistic flow fields is inherently more challenging. Additionally, factors such as measurement locations can drastically influence the estimated flow field. The role of the estimated flow field may be better understood as a predictor between state estimates, given the available data.

The methodological ideas presented here are quite general, and the iterative approach is suitable, in principle, for any application involving 2D images where no natural prediction model is available. The approach may also be applicable in settings where a dynamical model exists but requires a data-driven correction due to systematic misspecification.

One potential application of this approach is in nowcasting and weather radar image analysis. In fact, the optical flow method is already employed for prediction in many such applications [1, 33]. The KF has also been applied in similar contexts [35, 28]. Future work could further explore the practical use of multiframe optical flow estimation.

Appendix A. Filtering with spline basis functions. The iterative Kalman filter described in subsection 2.1 operates with the series of 2D images $\vec{x}_k$. If the dimensions of the images are even moderately high, for example, $N \times N$, handling or even storing the covariance matrices, which are of size $N^2 \times N^2$, becomes challenging in practice.

One practical solution to this problem is to use the dimension reduction KF introduced by [39] and later applied to dynamic X-ray images by [21].

The idea is to describe the state as

$$\vec{x}_k = \vec{\mu}_k + \mathbf{P}_k \vec{\alpha}_k, \tag{A.1}$$

where $\vec{\mu}_k$ represents the mean and $\mathbf{P}_k$ is the projection matrix that projects parameters $\vec{\alpha}_k$ from the low-dimensional subspace onto the full state space. In practical terms, we select the mean to be the KF prior $\vec{x}_k^{\text{pr}}$, and the projection matrix $\mathbf{P}_k = \mathbf{P}$ to be static.

In previous research [39, 21], we formed the static projection matrix $\mathbf{P}$, utilizing global basis functions, either through model-created "snapshots" or Gaussian processes. Here, we employ local basis functions based on B-splines, as discussed in the context of generalized additive models by [41].

In B-spline framework, piecewise polynomial basis functions $B_{i,p}(t)$ of degree $p+1$ on $t \in [0,1]$ are defined for $i = 0, \ldots, n$. For $p > 0$, the basis functions are defined recursively as

$$B_{i,p}(t) = \frac{t - t_i}{t_{i+p} - t_i} B_{i,p-1}(t) + \frac{t_{i+p+1} - t}{t_{i+p+1} - t_{i+1}} B_{i+1,p-1}(t), \tag{A.2}$$

where $0/0 = 0$ by definition. For $p = 0$, the basis functions are defined as

$$B_{i,0}(t) = \begin{cases} 1 & \text{if } t_i \le t < t_{i+1}, \\ 0 & \text{otherwise.} \end{cases}$$

A collection of K *breakpoints* is called a knot vector:

$$\vec{t} = [t_1, t_2, \ldots, t_K]^{\mathrm{T}}, \tag{A.3}$$

where $K = p + n + 2$ and the values of t_i satisfy the relation $0 = t_1 \le t_2 \le \cdots \le t_K = 1$.

Here, for 2D images, the B-spline basis matrices $\mathbf{B_x}$ and $\mathbf{B_y}$ are created for both the x- and y-direction of the image. The final projection matrix $\mathbf{P}$, the tensor-product basis to be used in Kalman filtering, is then obtained via Kronecker product:

$$\mathbf{P} = \mathbf{B_x} \otimes \mathbf{B_y}. \tag{A.4}$$

The total number of basis vectors is $r = (n+1)^2$. In a typical application, the number of basis vectors is selected much smaller than the size of the 2D image.

Appendix B. GEOS-Chem model. For creating synthetic satellite CO_2 experiments, we utilized the global chemical transport model GEOS-Chem version 12.9.1 (www.geos-chem.org). We conducted CO_2 simulations driven by the Modern-Era Retrospective Analysis for Research and Applications version 2 (MERRA2) from NASA/GMAO. This model does not include chemistry but incorporates atmospheric CO_2 fluxes from biomass burning (GFED4 [46]), biofuel burning [50], fossil fuel burning (Open-source Data Inventory for Atmospheric CO_2 emissions, ODIAC [30]), ocean exchange [45], and terrestrial biospheric exchange [2]. The simulations included 47 vertical levels with a horizontal grid resolution of 2 × 2.5 latitude/longitude.

REFERENCES

[1] G. Ayzel, M. Heistermann, and T. Winterrath, *Optical flow models as an open benchmark for radar-based precipitation nowcasting (rainymotion v0.1)*, Geosci. Model Dev., 12 (2019), pp. 1387–1402, https://doi.org/10.5194/gmd-12-1387-2019.

[2] D. F. Baker, R. M. Law, K. R. Gurney, P. Rayner, P. Peylin, A. S. Denning, P. Bousquet, L. Bruhwiler, Y.-H. Chen, P. Ciais, I. Y. Fung, M. Heimann, J. John, T. Maki, S. Maksyutov, K. Masarie, M. Prather, B. Pak, S. Taguchi, and Z. Zhu, *TransCom 3 inversion intercomparison: Impact of transport model errors on the interannual variability of regional CO_2 fluxes,* 1988-2003, Global Biogeochemical Cycles, 20 (2006), https://doi.org/10.1029/2004GB002439.

[3] S. Bonnet, A. Koenig, S. Roux, P. Hugonnard, R. Guillemaud, and P. Grangeat, *Dynamic X-ray computed tomography*, Proc. IEEE, 91 (2003), pp. 1574–1587.

[4] T. Brox, A. Bruhn, N. Papenberg, and J. Weickert, *High accuracy optical flow estimation based on a theory for warping*, in Computer Vision - ECCV 2004, T. Pajdla and J. Matas, eds., Springer, Berlin, Heidelberg, 2004, pp. 25–36, https://doi.org/10.1007/978-3-540-24673-2_3.

[5] T. Brox and J. Malik, *Large displacement optical flow: Descriptor matching in variational motion estimation*, IEEE Trans. Pattern Anal. Mach. Intell., 33 (2011), pp. 500–513, https://doi.org/10.1109/TPAMI.2010.143.

[6] T. A. Bubba, T. Heikkilä, H. Help, S. Huotari, Y. Salmon, and S. Siltanen, *Sparse dynamic tomography: A shearlet-based approach for iodine perfusion in plant stems*, Inverse Problems, 36 (2020), 094002, https://doi.org/10.1088/1361-6420/ab9c15.

[7] M. Burger, H. Dirks, L. Frerking, A. Hauptmann, T. Helin, and S. Siltanen, *A variational reconstruction method for undersampled dynamic X-ray tomography based on physical motion models*, Inverse Problems, 33 (2017), 124008, https://doi.org/10.1088/1361-6420/aa99cf.

[8] A. Chen, J. Mao, D. Ricciuto, J. Xiao, C. Frankenberg, X. Li, P. E. Thornton, L. Gu, and A. K. Knapp, *Moisture availability mediates the relationship between terrestrial gross primary production and solar-induced chlorophyll fluorescence: Insights from global-scale variations*, Glob. Change Biol., 27 (2021), pp. 1144–1156, https://doi.org/10.1111/gcb.15373.

[9] A. Descals, A. Verger, G. Yin, I. Filella, and J. Peñuelas, *Local interpretation of machine learning models in remote sensing with SHAP: The case of global climate constraints on photosynthesis phenology*, Int. J. Remote Sens., 44 (2023), pp. 3160–3173, https://doi.org/10.1080/01431161.2023.2217982.

[10] G. A. Einicke, *Iterative filtering and smoothing of measurements possessing Poisson noise*, IEEE Trans. Aero. Electron. Syst., 51 (2015), pp. 2205–2011, https://doi.org/10.1109/TAES.2015.140843.

[11] V. Elvira and E. Chouzenoux, *Graphical inference in linear-Gaussian state-space models*, IEEE Trans. Signal Process., 70 (2022), pp. 4757–4771, https://doi.org/10.1109/TSP.2022.3209016.

[12] L. Frenkel and M. Feder, *Recursive expectation-maximization (EM) algorithms for time-varying parameters with applications to multiple target tracking*, IEEE Trans. Signal Process., 47 (1999), pp. 306–320, https://doi.org/10.1109/78.740104.

[13] J.-P. Gastellu-Etchegorry, N. Lauret, T. Yin, L. Landier, A. Kallel, Z. Malenovskỳ, A. Al Bitar, J. Aval, S. Benhmida, J. Qi, G. Medjdoub, J. Guilleux, E. Chavanon, B. Cook, D. Morton, N. Chrysoulakis, and Z. Mitraka, *DART: Recent advances in remote sensing data modeling with atmosphere, polarization, and chlorophyll fluorescence*, IEEE J. Sel. Top. Appl., 10 (2017), pp. 2640–2649, https://doi.org/10.1109/JSTARS.2017.2685528.

[14] J. Gibson and O. Marques, *Optical Flow and Trajectory Estimation Methods*, 1st ed., SpringerBriefs in Computer Science, Springer International Publishing, Cham, 2016.

[15] M. S. Grewal and A. P. Andrews, *Applications of Kalman filtering in aerospace* 1960 *to the present [historical perspectives]*, IEEE Control Syst., 30 (2010), pp. 69–78, https://doi.org/10.1109/MCS.2010.936465.

[16] L. Guanter, C. Bacour, A. Schneider, I. Aben, T. A. van Kempen, F. Maignan, C. Retscher, P. Köhler, C. Frankenberg, J. Joiner, and Y. Zhang, *The TROPOSIF global sun-induced fluorescence dataset from the Sentinel-*5*P TROPOMI mission*, Earth Syst. Sci. Data, 13 (2021), pp. 5423–5440, https://doi.org/10.5194/essd-13-5423-2021.

[17] M. Gunia, M. Laine, O. Malve, K. Kallio, M. Kervinen, S. Anttila, N. Kotamäki, E. Siivola, J. Kettunen, and T. Kauranne, *Data fusion system for monitoring water quality: Application to chlorophyll-a in Baltic sea coast*, Environ. Modell. Softw., 155 (2022), 105465, https://doi.org/10.1016/j.envsoft.2022.105465.

[18] J. Hakkarainen, I. Ialongo, S. Maksyutov, and D. Crisp, *Analysis of four years of global* XCO_2 *anomalies as seen by Orbiting Carbon Observatory-*2, Remote Sens., 11 (2019), 850, https://doi.org/10.3390/rs11070850.

[19] J. Hakkarainen, I. Ialongo, and J. Tamminen, *Direct space-based observations of anthropogenic* CO_2 *emission areas from OCO-*2, Geophys. Res. Lett., 43 (2016), pp. 11,400–11,406, https://doi.org/10.1002/2016GL070885.

[20] J. Hakkarainen, A. Ilin, A. Solonen, M. Laine, H. Haario, J. Tamminen, E. Oja, and H. Järvinen, *On closure parameter estimation in chaotic systems*, Nonlin. Process. Geophys., 19 (2012), pp. 127–143, https://doi.org/10.5194/npg-19-127-2012.

[21] J. Hakkarainen, Z. Purisha, A. Solonen, and S. Siltanen, *Undersampled dynamic X-ray tomography with dimension reduction Kalman filter*, IEEE Trans. Comput. Imaging, 5 (2019), pp. 492–501, https://doi.org/10.1109/TCI.2019.2896527.

[22] B. K. Horn and B. G. Schunck, *Determining optical flow*, Artif. Intell., 17 (1981), pp. 185–203, https://doi.org/10.1016/0004-3702(81)90024-2.

[23] G. Janssens-Maenhout, B. Pinty, M. Dowell, H. Zunker, E. Andersson, G. Balsamo, J. L. Bézy, T. Brunhes, H. Bösch, B. Bojkov, D. Brunner, M. Buchwitz, D. Crisp, P. Ciais, P. Counet, D. Dee, H. Denier van der Gon, H. Dolman, M. R. Drinkwater, O. Dubovik, R. Engelen, T. Fehr, V. Fernandez, M. Heimann, K. Holmlund, S. Houweling, R. Husband, O. Juvyns, A. Kentarchos, J. Landgraf, R. Lang, A. Löscher, J. Marshall, Y. Meijer, M. Nakajima, P. I. Palmer, P. Peylin, P. Rayner, M. Scholze, B. Sierk, J. Tamminen, and P. Veefkind, *Toward an operational anthropogenic CO_2 emissions monitoring and verification support capacity*, Bull. AMS, 101 (2020), pp. E1439–E1451, https://doi.org/10.1175/BAMS-D-19-0017.1.

[24] M. Laine, N. Latva-Pukkila, and E. Kyrölä, *Analysing time-varying trends in stratospheric ozone time series using the state space approach*, Atmos. Chem. Phys., 14 (2014), pp. 9707–9725, https://doi.org/10.5194/acp-14-9707-2014.

[25] B. D. Lucas and T. Kanade, *An iterative image registration technique with an application to stereo vision*, in Proceedings of the 7th International Joint Conference on Artificial Intelligence - Volume 2, IJCAI'81, Morgan Kaufmann Publishers, San Francisco, 1981, pp. 674–679.

[26] A. Meaney, Z. Purisha, and S. Siltanen, *Tomographic X-ray Data of 3D Emoji*, preprint, https://arxiv.org/abs/1802.09397, 2018.

[27] T. Moon, *The expectation-maximization algorithm*, IEEE Signal Process. Mag., 13 (1996), pp. 47–60, https://doi.org/10.1109/79.543975.

[28] D. Nerini, L. Foresti, D. Leuenberger, S. Robert, and U. Germann, *A reduced-space ensemble Kalman filter approach for flow-dependent integration of radar extrapolation nowcasts and NWP precipitation ensembles*, Mon. Weather Rev., 147 (2019), pp. 987–1006, https://doi.org/10.1175/MWR-D-18-0258.1.

[29] Noveltis, Upv, Sron, Lsce, and Esa, *The TROPOSIF Global Sun-Induced Fluorescence Dataset from the TROPOMI Mission*, 2021, https://doi.org/10.5270/esa-s5p_innovation-sif-20180501_20210320-v2.1-202104.

[30] T. Oda, S. Maksyutov, and R. J. Andres, *The open-source data inventory for anthropogenic CO_2, version 2016 (ODIAC2016): A global monthly fossil fuel CO_2 gridded emissions data product for tracer transport simulations and surface flux inversions*, Earth Syst. Sci. Data, 10 (2018), pp. 87–107, https://doi.org/10.5194/essd-10-87-2018.

[31] G. P. Penney, P. G. Batchelor, D. L. G. Hill, D. J. Hawkes, and J. Weese, *Validation of a two- to three-dimensional registration algorithm for aligning preoperative CT images and intraoperative fluoroscopy images*, Med. Phys., 28 (2001), pp. 1024–1032, https://doi.org/10.1118/1.1373400.

[32] W. Peters, J. B. Miller, J. Whitaker, A. S. Denning, A. Hirsch, M. C. Krol, D. Zupanski, L. Bruhwiler, and P. P. Tans, *An ensemble data assimilation system to estimate CO_2 surface fluxes from atmospheric trace gas observations*, J. Geophys. Res.: Atmospheres, 110 (2005), https://doi.org/10.1029/2005JD006157.

[33] S. Pulkkinen, V. Chandrasekar, and T. Niemi, *Lagrangian integro-difference equation model for precipitation nowcasting*, J. Atmos. Ocean. Tech., 38 (2021), pp. 2125–2145, https://doi.org/10.1175/JTECH-D-21-0013.1.

[34] H. E. Rauch, C. T. Striebel, and F. Tung, *Maximum likelihood estimates of linear dynamic systems*, AIAA J., 3 (1965), pp. 1445–1450, https://doi.org/10.2514/3.3166.

[35] P. J. Rossi, V. Chandrasekar, V. Hasu, and D. Moisseev, *Kalman filtering–based probabilistic nowcasting of object-oriented tracked convective storms*, J. Atmos. Ocean. Tech., 32 (2015), pp. 461–477, https://doi.org/10.1175/JTECH-D-14-00184.1.

[36] S. Särkkä, *Bayesian Filtering and Smoothing*, Cambridge University Press, 2013.

[37] X. Shi, Z. Huang, W. Bian, D. Li, M. Zhang, K. Cheung, S. See, H. Qin, J. Dai, and H. Li, *Videoflow: Exploiting temporal cues for multi-frame optical flow estimation*, in 2023 IEEE/CVF International Conference on Computer Vision (ICCV), IEEE Computer Society, Los Alamitos, CA, 2023, pp. 12435–12446, https://doi.org/10.1109/ICCV51070.2023.01146.

[38] J. Smith, C. Birch, J. Marsham, S. Peatman, M. Bollasina, and G. Pankiewicz, *Evaluating pySTEPS optical flow algorithms for convection nowcasting over the maritime continent using satellite data*, Nat. Hazards Earth Syst. Sci., 24 (2024), pp. 567–582, https://doi.org/10.5194/nhess-24-567-2024.

[39] A. Solonen, T. Cui, J. Hakkarainen, and Y. Marzouk, *On dimension reduction in Gaussian filters*, Inverse Problems, 32 (2016), 045003, https://doi.org/10.1088/0266-5611/32/4/045003.

[40] A. Solonen, J. Hakkarainen, A. Ilin, M. Abbas, and A. Bibov, *Estimating model error covariance matrix parameters in extended Kalman filtering*, Nonlinear Process. Geoph., 21 (2014), pp. 919–927, https://doi.org/10.5194/npg-21-919-2014.

[41] A. Solonen and S. Staboulis, *On Bayesian Generalized Additive Models*, preprint, https://arxiv.org/abs/2303.02626, 2023.

[42] S. Springer, A. Glielmo, A. Senchukova, T. Kauppi, J. Suuronen, L. Roininen, H. Haario, and A. Hauptmann, *Reconstruction and segmentation from sparse sequential X-ray measurements of wood logs*, Appl. Math. Modern Challenges, 1 (2023), pp. 1–20, https://doi.org/10.3934/ammc.2023002.

[43] Y. Sun, C. Frankenberg, J. D. Wood, D. S. Schimel, M. Jung, L. Guanter, D. T. Drewry, M. Verma, A. Porcar-Castell, T. J. Griffis, L. Gu, T. S. Magney, P. Köhler, B. Evans, and K. Yuen, *OCO-*2 *advances photosynthesis observation from space via solar-induced chlorophyll fluorescence*, Science, 358 (2017), eaam5747, https://doi.org/10.1126/science.aam5747.

[44] R. Szeliski, *Computer Vision*, 2nd ed., Texts in Computer Science, Springer Nature, Cham, 2022.

[45] T. Takahashi, S. C. Sutherland, R. Wanninkhof, C. Sweeney, R. A. Feely, D. W. Chipman, B. Hales, G. Friederich, F. Chavez, C. Sabine, A. Watson, D. C. Bakker, U. Schuster, N. Metzl, H. Yoshikawa-Inoue, M. Ishii, T. Midorikawa, Y. Nojiri, A. Kölrtzinger, T. Steinhoff, M. Hoppema, J. Olafsson, T. S. Arnarson, B. Tilbrook, T. Johannessen, A. Olsen, R. Bellerby, C. Wong, B. Delille, N. Bates, and H. J. de Baar, *Climatological mean and decadal change in surface ocean* pCO_2*, and net sea-air* CO_2 *flux over the global oceans*, Deep Sea Research Part II: Topical Studies in Oceanography, 56 (2009), pp. 554–577, https://doi.org/10.1016/j.dsr2.2008.12.009.

[46] G. R. van der Werf, J. T. Randerson, L. Giglio, G. J. Collatz, M. Mu, P. S. Kasibhatla, D. C. Morton, R. S. DeFries, Y. Jin, and T. T. van Leeuwen, *Global fire emissions and the contribution of deforestation, savanna, forest, agricultural, and peat fires* (1997-2009), Atmos. Chem. Phys., 10 (2010), pp. 11707–11735, https://doi.org/10.5194/acp-10-11707-2010.

[47] S. Vedula, P. Rander, R. Collins, and T. Kanade, *Three-dimensional scene flow*, IEEE Trans. Pattern Anal. Mach. Intell., 27 (2005), pp. 475–480, https://doi.org/10.1109/TPAMI.2005.63.

[48] B. Weir, D. Crisp, C. W. O'Dell, S. Basu, A. Chatterjee, J. Kolassa, T. Oda, S. Pawson, B. Poulter, Z. Zhang, P. Ciais, S. J. Davis, Z. Liu, and L. E. Ott, *Regional impacts of COVID-*19 *on carbon dioxide detected worldwide from space*, Sci. Adv., 7 (2021), eabf9415, https://doi.org/10.1126/sciadv.abf9415.

[49] P. Yang, E. Prikaziuk, W. Verhoef, and C. van der Tol, *SCOPE* 2.0*: A model to simulate vegetated land surface fluxes and satellite signals*, Geosci. Model Dev., 14 (2021), pp. 4697–4712, https://doi.org/10.5194/gmd-14-4697-2021.

[50] R. Yevich and J. A. Logan, *An assessment of biofuel use and burning of agricultural waste in the developing world*, Global Biogeochem. Cycles, 17 (2003), https://doi.org/10.1029/2002GB001952.

[51] T. Yokota, Y. Yoshida, N. Eguchi, Y. Ota, T. Tanaka, H. Watanabe, and S. Maksyutov, *Global concentrations of* CO_2 *and* CH_4 *retrieved from GOSAT: First preliminary results*, SOLA, 5 (2009), pp. 160–163, https://doi.org/10.2151/sola.2009-041.

[52] Z. Zhang, J. M. Chen, Y. Zhang, and M. Li, *Improving the ability of solar-induced chlorophyll fluorescence to track gross primary production through differentiating sunlit and shaded leaves*, Agr. Forest Meteorol., 341 (2023), 109658, https://doi.org/10.1016/j.agrformet.2023.109658.